A space-fractional Bidomain framework for cardiac electrophysiology: 1D alternans dynamics

Nicole Cusimano[a,*], Luca Gerardo-Giorda[b,c], Alessio Gizzi[d]

[a]*Basque Center for Applied Mathematics, 48009 Bilbao, Spain*
[b]*Johannes Kepler University, 4040 Linz, Austria*
[c]*RICAM, Austrian Academy of Science, 4040 Linz, Austria*
[d]*Department of Engineering, Campus Bio-Medico University of Rome, 00128 Rome, Italy*

Abstract

Cardiac electrophysiology modelling deals with a complex network of excitable cells forming an intricated syncytium: the heart. The electrical activity of the heart shows recurrent spatial patterns of activation, known as cardiac alternans, featuring multiscale emerging behavior. On these grounds, we propose a novel mathematical formulation for cardiac electrophysiology modelling and simulation incorporating spatially non-local couplings within a physiological reaction-diffusion scenario. We formulate, in particular, a space-fractional Bidomain electrophysiological framework, extending and generalising similar works conducted for the Monodomain model. We characterise one-dimensional excitation patterns by performing an extended numerical analysis encompassing a broad spectrum of space-fractional derivative powers and various intra- and extra-cellular conductivities combinations. Our numerical study demonstrates that: (i) symmetry properties occur in the conductivity parameters space following the proposed theoretical framework; (ii) the degree of non-local coupling affects the onset and evolution of discordant alternans dynamics; (iii) the theoretical framework fully recovers classical formulations and is amenable for parametric tuning relying on experimental conduction velocity and action potential morphology.

Heart diseases affect most of the population worldwide. Irregular electrical patterns represent, still today, the primary factor leading to sudden cardiac death irrespective of the enormous

---

*Corresponding author
 Email address:* `nicole.cusimano@outlook.com` (Nicole Cusimano)

scientific and technological effort in understanding their intrinsic mechanisms. Mathematical and computational tools have undoubtedly been key players in this quest, and still are. Today's challenge is how to incorporate highly heterogeneous microscopic features into a reliable numerical tool that can be effectively used at the scale of a whole heart. We explore this aspect by proposing a generalised space-fractional Bidomain framework for modelling and simulation of cardiac electrophysiology in extended spatial domains. By enriching our previous efforts on this novel rationale [1], we demonstrate that the onset and evolution of irregular electrical patterns, such as cardiac alternans, are affected by the degree of non-local coupling. Our ultimate objective is to unveil novel critical mechanisms that can induce the onset cardiac arrhythmias in view of future clinical validation.

1. Introduction

Understanding the complex dynamics underlying the multiscale features of excitable biological media is becoming of paramount importance in cardiac modelling, especially for personalised medical treatment [2, 3]. The enormous effort that has been made to this day in theoretical, experimental, and clinical research in cardiac electrophysiology still has not been able to fully elucidate important issues and underlying mechanisms, such as cell-cell communication, emerging behaviors, irregular rhythms (alternans), and arrhythmias onset [4, 5]. Cardiac alternans, in particular, are due to increased dispersion of repolarisation leading to large variations in refractory period and conduction velocity that, in turn, can induce arrhythmias onset (see, e.g., [6, 7, 8, 9] and references therein). Dispersion of action potential duration (APD) has been shown to develop during fast pacing resulting in the alternation of the excitation wave, even when the period remains constant. Such complex phenomena underlie life-threatening mechanisms still requiring a clear elucidation.

In such a scenario, mathematical modelling provides a fundamental tool for the investigation and the advanced mechanistic explanation of strongly coupled nonlinear phenomena due to the intrinsic spatio-temporal coupling in cardiac tissue (e.g., [10, 11, 12]). The Bidomain and Monodomain theoretical frameworks, in particular, have been widely used to assess traveling wave features, recovering several experimental pieces of evidence but still lacking a precise understanding of the critical conditions leading to recurrent cardiac alternans pat-

2

terns [13, 14, 15, 16]. Recently, these models have been further generalised to assess data assimilation and uncertainty quantification procedures that represent a key tool to reconstruct and predict excitation patterns in cardiac tissue with high fidelity [17, 18, 19, 20, 21, 22].

The Bidomain model [23] of cardiac tissue is a continuous description in which the conductive medium is seen as a functional syncytium of electrically coupled cells. This model assumes cardiac tissue to be the union of two overlapping and continuous domains (namely, the intra- and extra-cellular domains) connected by the cellular membrane. Under these assumptions, macroscopic variations of electrical intra- and extra-cellular potentials are then derived via Ohm's law, the conservation of current and charge, and by assuming only membrane related sources in the two cellular spaces [24].

Under the assumption of equal anisotropy ratio (i.e., proportionality in the conductivity tensors of the two spatial domains - see Section 2 for further details) the Bidomain system of equations reduces to the so-called Monodomain formulation [24]. While this assumption is known to be unrealistic, many studies have shown that often differences between Bidomain and Monodomain results are small enough to be ignored for many applications [25] and the Monodomain has hence been preferred and extensively used in cardiac simulations due to its lower computational cost. However, there are some important exceptions in which the Monodomain formulation does not suffice to model the dynamics of interest, such as in the case of simulations involving applied currents (e.g., virtual electrode simulations and defibrillation protocols) [26, 27, 28] or in reproducing complex alternans patterns within a realistic cardiac domain [29]. Unequal anisotropy ratios and the fact that currents in the extracellular domain influence the dynamics of the transmembrane potential are indeed key factors in reproducing the experimentally observed features of electrical propagation in these settings, thus still making the Bidomain a model of considerable interest. In the present contribution we refer, in particular, to quasi-1D cardiac anatomical structures, e.g., Purkinje fibres or single muscular fibres, as benchmark study. These structures range among several centimeters and support multiple complex alternans states [30, 31].

While tremendous progress has been made over the years via results produced either with the Monodomain or the Bidomain models, these formulations are (as all mathematical models) approximations and, as such, have inherent and well-known limitations. Considerable effort has been made in recent years in order to generalise these models as to account for complex spatio-temporal behaviour observed experimentally and/or to incorporate into the mathematical descriptions the effects of increasing structural complexity (unveiled by the quick progress in

modern imaging techniques). A partial list covers: ephaptic coupling [32, 33], a nonlinear porous-medium approach [34, 35, 29], non-Ohmic conduction [36, 37], space-fractional [38, 39, 40, 1, 41] and time-fractional electrophysiology [42, 43], and complex order [44, 45] approaches.

Transport phenomena in highly heterogeneous environments can naturally exhibit features that deviate from classical diffusion simply due to the structural complexity of the medium in which the phenomena take place. When studying electrical propagation in cardiac tissue, microscopic structural heterogeneity is often neglected in modelling electrical propagation at the macroscopic scale, thus hindering the investigation and characterisation of cardiac conduction modulation due to the composite tissue microstructure.

Bueno-Orovio et al. [38] were the first to propose a space-fractional Monodomain formulation to tackle this issue, justifying the use of fractional powers of a classical diffusion operator by making a connection between Riesz potential theory and the total electrical field associated to a heterogeneous biological medium like cardiac tissue. In this interpretation, a reduction in the fractional exponent of the space-fractional formulation corresponds to an enhancement of the perturbations that secondary sources (i.e., tissue inhomogeneities) give to electrical potential otherwise associated with a uniform volume conductor. Discontinuities are present on a variety of scales, both in the intracellular and the extracellular domains, suggesting that alternative modelling frameworks (such as the one considered here), which are able to account for the multi-scale nature of the observed phenomenon without the need of a detailed resolution of the spatial scale all the way down to the microscopic level, might provide enhanced or complementary understanding into complex mechanisms that traditional approaches cannot unravel. Moreover, if the structural heterogeneity argument already makes sense in non-diseased hearts, it is even more valid when considering pathological conditions (e.g., fibrosis, ischaemia, myocyte disarray, etc.).

In this manuscript, we consider the space-fractional approach and build on the motivations proposed in the original work by Bueno-Orovio et al. [38] to formulate a two-domain generalisation of the fractional models previously studied in these settings: the *fractional Bidomain* (FBD). While the assumption of fractional diffusion in the extracellular domain could be attributed to the composite microstructure of cardiac tissue (i.e., the presence of blood vessels and cardiac interstitial cells, including endothelial, smooth muscle cells, pericytes, peripheral nerves and fibroblasts, in addition to cardiac myocytes), the assumption of fractional diffusion in the intercellular domain could be associated to the role played by gap junctions in modulating inter-cellular signal propagation [46, 47] as well

as to the complexity of the intra-cellular space through which chemical species (and calcium ions in particular) diffuse [48, 49].

We introduce the novel model and make a preliminary study of the complex spatio-temporal dynamics resulting from the use of non-local fractional diffusive operators in one or both cellular domains of the Bidomain formulation. In the numerical simulations proposed here, we only consider the one-dimensional (1D) case, laying the foundations for future work in this direction in multiple spatial dimensions and more realistic settings. Although simplistic, we stress that the proposed simulations already offer interesting new scenarios compared to our previous work on non-local cardiac electrophysiology in which the fractional Monodomain was considered [1]. In fact, contrary to the case of the standard Bidomain in 1D (where inevitable proportionality of scalar conductivities in the intra- and extra-cellular spaces implies that results can be reproduced via an equivalent Monodomain model), introducing different degrees of non-locality in the two domains results in spatio-temporal characteristics of the excitation wave propagation that cannot be simply obtained via an equivalent fractional Monodomain formulation.

In Section 2 we introduce the mathematical formulation of the FBD model, we define the boundary conditions and the ionic model considered in this work, we outline the numerical approach adopted and define the stimulation protocols of our numerical simulations. Our results are presented and discussed in detail in Section 3, while conclusions are drawn in Section 4.

2. Methods

2.1. The fractional Bidomain formulation

Letting V, u_i, u_e denote the transmembrane, intra- and extra-cellular potentials, respectively, then $u_i = V + u_e$ and the parabolic-parabolic formulation of the standard Bidomain is as follows:

$$
\begin{aligned}
\chi \left(C_m \frac{\partial V}{\partial t} + I_{\text{ion}} \right) &= \nabla \cdot (\sigma_i \nabla u_i) \\
\chi \left(C_m \frac{\partial V}{\partial t} + I_{\text{ion}} \right) &= -\nabla \cdot (\sigma_e \nabla u_e)
\end{aligned}
\tag{1}
$$

where χ is the cell surface-to-volume ratio, C_m is the cell membrane capacitance, I_{ion} is the ionic current (described by the specific ionic model adopted), and σ_i, σ_e are the conductivity tensors for the intra- and extra-cellular domains, respectively.

Letting $\mathscr{L}_i$ denote the diffusive operator $\mathscr{L}_i = (-\nabla \cdot \boldsymbol{\sigma}_i \nabla)$ (with an analogous definition for $\mathscr{L}_e$), in this work we consider the following space-fractional generalisation of (1):

$$\chi \left(C_m \frac{\partial V}{\partial t} + I_{\text{ion}} \right) = -\mathscr{L}_i^{s_i}[u_i],$$
$$\chi \left(C_m \frac{\partial V}{\partial t} + I_{\text{ion}} \right) = \mathscr{L}_e^{s_e}[u_e], \tag{2}$$

where $\mathscr{L}_i^{s_i}$ and $\mathscr{L}_e^{s_e}$ are fractional powers (defined in spectral sense) of the diffusion operators $\mathscr{L}_i$ and $\mathscr{L}_e$, with fractional exponents s_i and s_e ($s_i, s_e \in (0,1]$) representing the effect of structural heterogeneity for the intra- and extra-cellular domains, respectively [40]. Specifically, letting $\{\mu_j, \varphi_j\}_{j=1}^{\infty}$ be the set of eigenvalues and corresponding orthonnormal eigenfunctions of the operator $\mathscr{L}_i$ on the spatial domain Ω (with suitable homogeneous boundary conditions), the spectral theorem defines fractional powers $\mathscr{L}_i^{s_i}$ as

$$\mathscr{L}_i^{s_i}[f] = \sum_{j=1}^{\infty} \mu_j^{s_i} \hat{f}_j \varphi_j, \quad \text{with} \quad \hat{f}_j := \int_{\Omega} f \varphi_j,$$

$\forall f \in L^2(\Omega)$ such that $\sum_j \mu_j^{2s_i} |\hat{f}_j|^2 < \infty$. Analogous definition applies to $\mathscr{L}_e^{s_e}$.

Note that, when a fractional exponent is equal to one, then the considered fractional power is nothing but the standard diffusion operator in that particular domain.

Some considerations are in order. Due to the linearity of the spectral fractional powers of the considered elliptic operators, similarly to the standard case, system (2) can be formulated in an equivalent "parabolic-elliptic" form, only involving V and u_e, which we will refer to as FBD in the rest of this manuscript:

$$\chi \left(C_m \frac{\partial V}{\partial t} + I_{\text{ion}} \right) = -\mathscr{L}_i^{s_i}[V] - \mathscr{L}_i^{s_i}[u_e], \tag{3}$$

$$0 = -\mathscr{L}_i^{s_i}[V] - (\mathscr{L}_i^{s_i} + \mathscr{L}_e^{s_e})[u_e]. \tag{4}$$

Under the assumptions $s_i = s_e = s$ and $\boldsymbol{\sigma}_e = \lambda \boldsymbol{\sigma}_i$ for some $\lambda > 0$ (i.e., equal anisotropy ratio), by following the same steps of the typical Bidomain to Monodomain simplification in the standard case (and by using linearity of the considered fractional operators) one derives the following fractional Monodomain equation:

$$\chi \left(C_m \frac{\partial V}{\partial t} + I_{\text{ion}} \right) = -\frac{\lambda^s}{1 + \lambda^s} \mathscr{L}_i^s[V]. \tag{5}$$

6

In fact, under these hypotheses, $\mathscr{L}_e^s = \lambda^s \mathscr{L}_i^s$ and hence from (4) we find

$$\mathscr{L}_i^s[u_e] = -\frac{1}{1+\lambda^s}\mathscr{L}_i^s[V]. \tag{6}$$

At this point, a mere substitution of (6) into (3) gives (5).

In the scalar case, when σ_i and σ_e are assumed to be constant throughout the domain, $\sigma_e = \lambda \sigma_i$ always holds, independently from the particular values of the two conductivities. Hence, in these settings the FBD formulation can always be reduced to the fractional Monodomain, provided that the fractional exponents s_i and s_e coincide. However, when $s_i \neq s_e$, by using $\mathscr{L}_e^{s_e} = \lambda^{s_e} \mathscr{L}_i^{s_e}$ in (4) we can only obtain

$$0 = -\mathscr{L}_i^{s_i}[V] - (\mathscr{L}_i^{s_i} + \lambda^{s_e}\mathscr{L}_i^{s_e})[u_e],$$

and the fractional Monodomain simplification no longer follows.

2.2. *Introducing stimuli and boundary conditions*

In order to trigger the propagation of action potentials, electrical stimuli are typically introduced both in the Bidomain formulation and in the boundary conditions. In the standard parabolic-elliptic formulation one has:

$$\chi\left(C_m\frac{\partial V}{\partial t} + I_{\mathrm{ion}}\right) - \mathscr{L}_i[u_i] = I_i^{(\mathrm{vol})}, \tag{7}$$

$$\mathscr{L}_i[u_i] + \mathscr{L}_e[u_e] = I_{tot}^{(\mathrm{vol})}, \tag{8}$$

where $I_{tot}^{(\mathrm{vol})} = I_i^{(\mathrm{vol})} + I_e^{(\mathrm{vol})}$ is the sum of (time-dependent) intra- and extra-cellular stimuli per unit volume, and the boundary conditions involve the specification of currents per unit area applied across the boundary, i.e.,

$$\mathbf{n}\cdot(\sigma_i\nabla u_i) = I_i^{(\mathrm{surf})}, \qquad \mathbf{n}\cdot(\sigma_e\nabla u_e) = I_e^{(\mathrm{surf})}.$$

The compatibility condition

$$\int_\Omega I_{tot}^{(\mathrm{vol})}dx + \int_{\partial\Omega}\left(I_i^{(\mathrm{surf})} + I_e^{(\mathrm{surf})}\right)dS = 0$$

is then necessary in order to ensure that the above singular system has a solution (actually an infinite number of them). Often in practice one assumes $I_{tot}^{(\mathrm{vol})} = I_i^{(\mathrm{surf})} = I_e^{(\mathrm{surf})} \equiv 0$ so that the compatibility condition is ensured. Note that this assumption does not mean that the extracellular stimulus per unit volume is zero

but rather $I_e^{(\text{vol})} = -I_i^{(\text{vol})}$ at every point in space and for all times [50]. This will be used in the rest of this work and notation will be simplified by using I_{stim} instead of $I_i^{(\text{vol})}$.

Moreover, by assuming $I_i^{(\text{surf})} = I_e^{(\text{surf})} = 0$ the boundary conditions of the problem correspond to zero-flux conditions in the two domains. This is compatible with the use of spectral fractional operators, where boundary conditions determine the spectrum and the eigenbasis of the operators considered, and does not require any special treatment (contrary to the case of inhomogeneous boundary conditions - see, e.g., [51]). In one spatial dimension, these boundary conditions reduce to homogeneous Neumann conditions for both u_e and V.

2.3. The ionic model

Whether fractional or standard, the Bidomain model is coupled at each point in space via the I_{ion} term to a system of ordinary differential equations describing excitability at the single cell level, i.e., how ionic properties and concentrations change in response to electrical stimulation in various cell compartments and via the opening and closing of specialised ionic channels in the cell membrane. For the results presented in this work, we use in our simulations the Beeler-Reuter ionic model [52]. We chose this particular model because it is biophysically grounded (thus allowing a direct connection between some of its variables, e.g., the calcium concentration, and quantities that are experimentally observable) and because this model is known to reproduce already various features of ventricular action potential without being overly complex and hence without requiring very large computation times. However, the methodology proposed here is independent from the particular choice of ionic model, and could be employed in a rather straightforward manner for the study of fractional tissue dynamics in combination with different levels of detail in the single cell response. Nevertheless, depending on the nature of the ionic model considered, some additional parameter tuning might be necessary in order to recover desirable features of spatio-temporal propagation of excitation waves in the fractional settings (an aspect that is surely very relevant, for example, in the case of phenomenological models [1, 22]).

2.4. Numerical solution

As in this preliminary study simulations are only performed in 1D, numerical computations can be simplified by exploiting the Fourier spectral method [53] (which has the same computational cost in the standard and the fractional cases) as follows.

1. We observe that the operators $\mathcal{L}_e$ and $\mathcal{L}_i$ coupled to homogeneous Neumann boundary conditions have the same eigenfunctions $\{\varphi_j\}_{j=1}^{\infty}$ and that the eigenvalues $\{\eta_j\}_{j=1}^{\infty}$ of $\mathcal{L}_e$ and $\{\mu_j\}_{j=1}^{\infty}$ of $\mathcal{L}_i$ are such that $\forall j$

$$\eta_j = \lambda \mu_j,$$

   where $\lambda > 0$ is such that $\sigma_e = \lambda \sigma_i$.

2. We write all functions in terms of the Fourier basis:

$$V(x,t) = \sum_{j=1}^{\infty} \hat{V}_j(t)\varphi_j(x), \quad u_e(x,t) = \sum_{j=1}^{\infty} \hat{u}_{ej}(t)\varphi_j(x),$$

$$g(x,t) = \sum_{j=1}^{\infty} \hat{g}_j(t)\varphi_j(x),$$

   where "hats" denote Fourier coefficients, and $g := -\chi I_{\text{ion}} + I_{\text{stim}}$.

3. We use the fact that $\mathcal{L}_i^{s_i}\varphi_j = \mu_j^{s_i}\varphi_j, \forall j$ (with analogous relationship for the extracellular fractional diffusion operator) and rewrite the FBD as

$$\chi C_m \sum_{j=1}^{\infty} \frac{\partial \hat{V}_j}{\partial t}\varphi_j + \sum_{j=1}^{\infty} \mu_j^{s_i}\hat{V}_j\varphi_j + \sum_{j=1}^{\infty} \mu_j^{s_i}\hat{u}_{ej}\varphi_j = \sum_{j=1}^{\infty} \hat{g}_j\varphi_j$$

$$\sum_{j=1}^{\infty} \mu_j^{s_i}\hat{V}_j\varphi_j + \sum_{j=1}^{\infty} (\mu_j^{s_i} + \eta_j^{s_e})\hat{u}_{ej}\varphi_j = 0.$$

4. We exploit orthonormality of the basis $\{\varphi_j\}$ to obtain for each j a system of equations independent from all other indices, i.e.,

$$\chi C_m \frac{\partial \hat{V}_j}{\partial t}(t) + \mu_j^{s_i}\hat{V}_j(t) + \mu_j^{s_i}\hat{u}_{ej}(t) = \hat{g}_j(t)$$

$$\mu_j^{s_i}\hat{V}_j(t) + (\mu_j^{s_i} + \eta_j^{s_e})\hat{u}_{ej}(t) = 0.$$

5. By using a semi-implicit scheme with uniform time step Δt for the discretisation of the systems above, at each time step n we get

$$\begin{bmatrix} \frac{\chi C_m}{\Delta t} + \mu_j^{s_i} & \mu_j^{s_i} \\ \mu_j^{s_i} & \mu_j^{s_i} + \eta_j^{s_e} \end{bmatrix} \begin{bmatrix} \hat{V}_j^{(n+1)} \\ \hat{u}_{ej}^{(n+1)} \end{bmatrix} = \begin{bmatrix} \frac{\chi C_m}{\Delta t}\hat{V}_j^{(n)} + \hat{g}_j^{(n)} \\ 0 \end{bmatrix},$$

which can be solved explicitly via substitution giving

$$\hat{u}_{ej}^{(n+1)} = -\frac{\mu_j^{s_i}}{\mu_j^{s_i} + \eta_j^{s_e}}\hat{V}_j^{(n+1)},$$ (9)

$$\hat{V}_j^{(n+1)} = \frac{1}{\frac{\chi C_m}{\Delta t} + \mu_j^{s_i} - \frac{\mu_j^{2s_i}}{\mu_j^{s_i} + \eta_j^{s_e}}}\left(\frac{\chi C_m}{\Delta t}\hat{V}_j^{(n)} + \hat{g}_j^{(n)}\right).$$ (10)

6. As we are working with zero-flux boundary conditions, the Fourier basis functions are cosines and the first eigenvalue for both operators is zero. Hence, for $j = 1$ the above must be corrected. In particular, for the transmembrane potential we have

$$\hat{V}_1^{(n+1)} = \hat{V}_1^{(n)} + \frac{\Delta t}{\chi C_m}\hat{g}_1^{(n)}.$$

On the other hand, due to the singular nature of the problem, u_e is only defined up to a constant. We hence define $\hat{u}_{e1}$ so that $\int_\Omega u_e dx = 0$. Specifically, letting $\widetilde{u_e}^{(n)} := \sum_{j=2}^\infty \hat{u}_{ej}^{(n)}\varphi_j$ we set

$$\hat{u}_{e1}^{(n)} = \frac{-\int_\Omega \widetilde{u_e}^{(n)}dx}{\int_\Omega \varphi_1 dx}.$$

7. All computations were done by considering the discrete cosine transform and a number of basis functions equal to the number of mesh points in the spatial discretisation grid.

As it is evident from equations (9) and (10), in the simplified settings considered here, there is a clear unidirectionality between transmembrane potential and extracellular potential in the solution of the problem. While the extracellular potential solution is directly determined by the transmembrane potential at each time step, the converse is not true and only the spectrum of the extracellular diffusion operator (rather than the actual extracellular potential solution) comes into play in (10). For this particular reason, other than providing in the Appendix an example of the temporal profile of both V and u_e for some selected parametric combinations, in the rest of this work we will only focus on the spatio-temporal dynamics of V since all variations in the behaviour of u_e could be directly brought back to corresponding variations in V, due to (9). We stress however that in general this unidirectionality does not hold and a truly bidirectional feedback between

10

the two electrical potentials is observed. For example, it would be enough for the boundary conditions not to be exactly the same for V and u_e (typically the case in two- or three-dimensional spatial simulations), and expressing both solutions in terms of the same eigenfunctions would no longer be possible. Obviously, in the general case the simplified numerical approach adopted here must be revisited and possibly alternative (but equivalent) formulations of the fractional operators (with corresponding solution approaches - e.g., see [40]) might have to be implemented.

Finally, we notice that the term involving the eigenvalues of the fractional diffusion operators in (10) can be rewritten as

$$\mu_j^{s_i} - \frac{\mu_j^{2s_i}}{\mu_j^{s_i} + \eta_j^{s_e}} = \frac{\mu_j^{s_i} \eta_j^{s_e}}{\mu_j^{s_i} + \eta_j^{s_e}},$$

which shows that (in the considered simplified settings) there is symmetry in the dependence of the transmembrane potential V from the eigenvalues of $\mathscr{L}_i^{s_i}$ and $\mathscr{L}_e^{s_e}$. Moreover, due to the fact that the eigenvalues of these fractional operators are fractional powers of

$$\eta_j = \sigma_e \left(\frac{j\pi}{L} \right)^2, \qquad \mu_j = \sigma_i \left(\frac{j\pi}{L} \right)^2,$$

where L is the 1D cable length, then it can be expected that the results obtained with a particular combination of fractional exponents and conductivities can also be obtained with the "mirror" parameterisation of the model, i.e., when swapping s_i with s_e and σ_i with σ_e. See further discussion on this in Section 3.1.

2.5. Protocols

Cable excitation was triggered via the application of a sufficiently strong stimulus. Each applied stimulus lasted for 1 ms, was injected on a small region (of size 0.05 cm independently from the cable length) at the left end of the domain, and the stimulus amplitude was equal to 100 mA·cm^{-3}.

Activation and recovery times for all simulations were computed via a fixed threshold set equal to roughly 90% of standard full repolarisation (-75 mV). At all points in space, AP duration (APD, or more precisely APD$_{90}$) is computed as the difference between the corresponding recovery and activation times. Mean conduction velocity (CV) was always measured on the central portion of the domain equal to half the domain size (namely, on 25% to 75% of the cable length).

This quantity was computed as the reciprocal of the coefficient obtained via a linear least squares fit of the activation times (i.e., isochrones of the wavefront) of all mesh points in the considered region.

The first set of simulations considers a cable of length $L = 3$ cm paced at a fixed basic cycle length (BCL) of 1000 ms until steady-state is reached. When measuring the mean CV, steady-state was defined as an absolute relative error below 1% between consecutive beats. In the alternans study discussed below, steady-state was reached when the absolute difference between the APD of two consecutive odd beats and two consecutive even beats was below 0.01 ms. The objective of this first set of simulations was to study the dependence of the conduction velocity from σ_i and σ_e for various combinations of the fractional parameters s_i and s_e.

The length of the cable is then increased (to $L = 6$ cm and $L = 9$ cm) and the onset of concordant and/or discordant alternans is assessed in different settings via a dynamic restitution protocol.

Cardiac alternans refers to beat-to-beat alternation in the APD with a repeated "long-short" pattern as stimulation progresses. Alternans can be concordant (CA) when the APD at all points in the domain follows the same pattern, or discordant (DA) when alternation is out-of-phase in different regions of the spatial domain. In the latter case, the intermediate regions (points in 1D) where APD does not change in subsequent beats are referred to as nodal lines (or simply nodes). In the dynamic restitution protocol, the cable is initially paced at a large BCL and pacing frequency is progressively increased (by gradually reducing the pacing BCL) until failure in propagation is observed (i.e., 2:1 response is recorded). At each considered BCL the cable is paced until APD steady-state is reached before considering the next (reduced) BCL.

All simulations were performed in MATLAB (R2017b, The MathWorks Inc., Natick, Massachusetts, US) on the high performance computing cluster Radon1 of the Johann Radon Institute for Computational and Applied Mathematics (RICAM) in Linz, Austria, and all results were post-processed on a 2.5GHz Intel Core i5 processor. Radon1 is a high performance computing cluster with 1168 computing cores and 10.7 TB of memory.

A rough number of the numerical simulations performed for this work and an estimate of the computation time required by each of them is given in Table A.1. Fortunately, due to the independence of each parametric combination considered, parallel computing could be used in order to run simultaneously multiple simulations, thus significantly reducing the total computation time.

3. Results

3.1. CV surface and isolines

Since the introduction of space-fractional diffusion affects both spatial and temporal features of the propagating action potential, including the CV of the excitation front (see e.g., [54]), in the first set of simulations we studied how CV varies as a function of σ_i and σ_e for various combinations of the fractional exponents s_i and s_e. Figure 1 a) shows the projection of the CV surface computed for $s_i = s_e = 1$ (i.e., standard diffusion in both domains) onto the (σ_i, σ_e) plane, highlighting a particular level set, namely the CV $= 49.5$ cm s^{-1} isoline. Without loss of generality, this isoline has been considered as a reference (and labelled CV$_{\text{ref}}$) for comparing results in the various non-local settings considered, that is, to match CV for the various combinations of s_i and s_e analysed in this section. However, we have also performed the analysis proposed here with refined mesh sizes and considering both smaller and larger reference values of the CV for comparison between different parameter sets. While no qualitative differences were observed in terms of CV surface shape and isoline position (results not shown), richer dynamical behaviour could be observed at lower CV when analysing alternans dynamics and node formation (see comments at the end of Section 3.3).

Notice that in the standard case the units for both conductivities are mS$\cdot$cm^{-1}, but in presence of fractional exponents strictly smaller than one, physical units for the conductivity parameters of the corresponding fractional operators should be rescaled accordingly in order to ensure balance in the various terms involved in the FBD model. This is assumed always to be the case and to avoid the use of unnecessarily heavy notation, throughout this section we will not report units for σ_i nor σ_e.

Figure 1 b) illustrates the specific combinations of the fractional exponents considered here. While green combinations are points for which $s_i = s_e$, and as such the corresponding results could be derived by an equivalent fractional Monodomain formulation as discussed in Section 2.1, off-diagonal combinations (red and black points) truly provide novel insights and the corresponding results could not be produced without the proposed FBD model. Notice that red points are mirror images of the points in black (with respect to the diagonal $s_i = s_e$). Due to the simplified settings in which the problem has been formulated, there is a symmetry in the role played by the conductivities σ_i and σ_e, when the values of s_i and s_e are swapped (as mentioned in Section 2.4). Therefore, numerical simulations were only performed for green and black points, but results could be extended also to red combinations via symmetry.
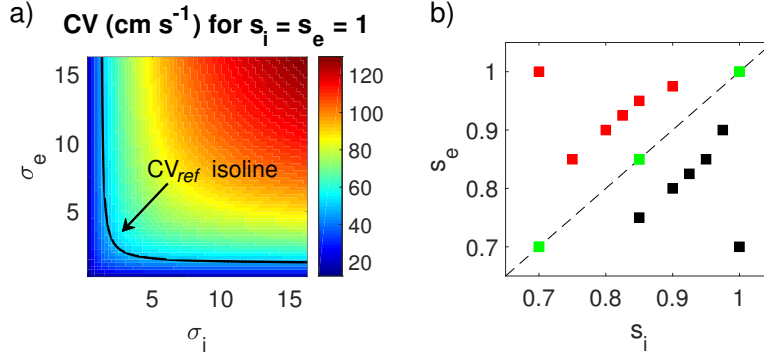
Figure 1: a) Projection of CV surface for $s_i = s_e = 1$ onto the (σ_i, σ_e) plane. The black line indicates the CV_{ref} isoline. b) Combinations of the fractional parameters s_i and s_e considered in this work. Red points indicate mirror images with respect to the $s_i = s_e$ diagonal (dashed line) of black combinations of the fractional exponents. Numerical simulations were only performed for green and black points but results could be extended also to red combinations via symmetry of the considered problem (see main text for discussion).

As an illustrative example of the analytical symmetry, in Figure 2 a) we plot the CV surface projection onto the (σ_i, σ_e) plane for $s_i = 0.95$, $s_e = 0.85$ (left) and its mirror combination $s_i = 0.85$, $s_e = 0.95$ (right). The same reference isoline is indicated in the two plots with the color black and red, respectively, and then both lines are plotted on the same diagram in Figure 2 b) for better visualisation purposes. Here, we also select two particular combinations of conductivities lying on the black isoline (labelling them with A and B, respectively) and use the same letters to identify the pairs of σ_i and σ_e on the red isoline that give the exact same results due to the symmetric nature of the problem.

Figure 3 shows differences in the CV surface and in the location of the same isoline for four different combinations of the fractional parameters:

$$
\begin{aligned}
\text{(top left)} \quad s_i &= s_e = 1, \\
\text{(top right)} \quad s_i &= s_e = 0.85, \\
\text{(bottom left)} \quad s_i &= 0.9 \quad \text{and} \quad s_e = 0.8, \\
\text{(bottom right)} \quad s_i &= 1 \quad \text{and} \quad s_e = 0.7.
\end{aligned}
$$

In all cases, as it is natural to expect, the CV increases smoothly and monotonically as the conductivities increase, and (in line with what observed for the fractional Monodomain [1]) the increase is much more gradual when considering smaller fractional exponents.
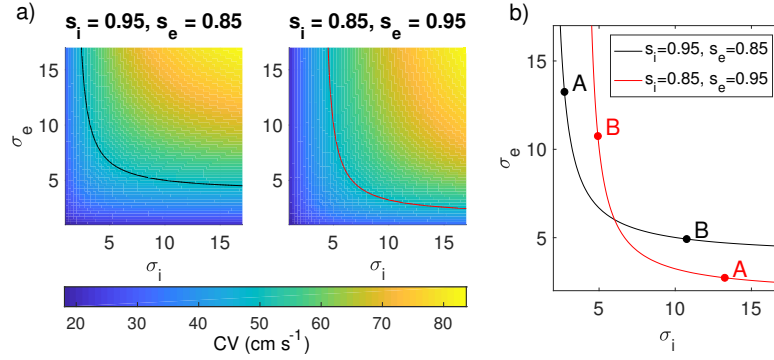
14

Figure 2: a) CV surface projections and location of the CV_{ref} isoline for $s_i = 0.95, s_e = 0.85$ and its mirror parameter combination ($s_i = 0.85, s_e = 0.95$). b) Identification of two particular (σ_i, σ_e) pairs (labelled A and B, respectively) on the considered isoline for $s_i = 0.95, s_e = 0.85$ (black) and corresponding (σ_i, σ_e) pairs on the isoline for $s_i = 0.85, s_e = 0.95$ (red).

Moreover, when $s_i = s_e = s$ (top row of Figure 3) there is symmetry with respect to the main diagonal $\sigma_i = \sigma_e$ (following from the discussion at the end of Section 2.4) and the corresponding surfaces could be ordered according to the fractional parameter s as they do not intersect. However, for mixed combinations $s_i \neq s_e$ (bottom row of Figure 3) non-linear effects emerge, and reciprocal positions of the considered surfaces (and their corresponding level sets) are no longer preserved in the entire space. Additional discussion in this regard is provided in the next subsection. Note that, in order to locate the same isoline for all considered combinations of s_i and s_e, the region of parameters (σ_i, σ_e) explored had to be suitably adjusted as evident from the four panels.

An illustrative example of action potential and extra-cellular potential profile for the above-mentioned four combinations of fractional exponents is given in Figure A.8 in the Appendix and the particular pairs of conductivities selected (in order to recover the same CV in all cases) are reported in Table A.3.

In Figure 4, the reference isoline CV_{ref} is drawn on the same plot for all considered combinations of fractional parameters listed in the legend (and also illustrated in the top right diagram with the corresponding colours to aid visualisation). Recall that, in light of the discussion previously made, for all combinations of fractional parameters, isolines corresponding to mirror parameter combinations could be easily obtained by simply reflecting the relevant isolines with respect to the diagonal $\sigma_i = \sigma_e$.
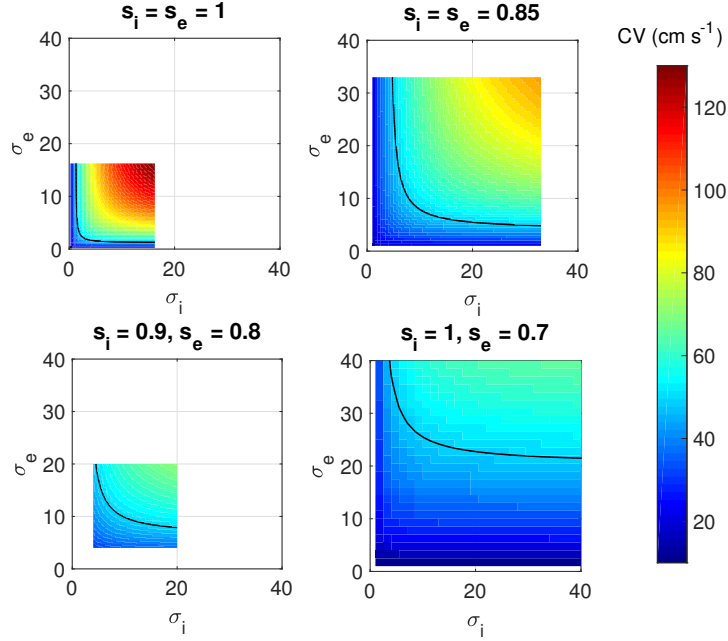
15

Figure 3: CV surface projection onto (σ_i, σ_e) space for four different (non-symmetric) combinations of the fractional parameters. In all plots, the black line indicates the CV_{ref} isoline.

3.2. CV fitting

In light of the large number of simulations performed for this study and to further elucidate the dependency of the CV from the FBD parameters, we found that (in the considered simplified settings) the CV can be described as a function of the conductivities and of the fractional exponents by the following analytic expression:

$$CV(\sigma_i, \sigma_e, s_i, s_e) = a_{s_i,s_e} \left(\frac{\sigma_i^{s_i} \sigma_e^{s_e}}{b_{s_i,s_e} \sigma_i^{s_i} + \sigma_e^{s_e}} \right)^{\frac{1}{s_i + s_e}}, \qquad (11)$$

where a_{s_i,s_e}, b_{s_i,s_e} are two positive constants depending on the fractional exponents.

Specific values of a and b for some selected combinations (s_i, s_e) with corresponding 95% confidence intervals (CI) are shown in Table A.2, together with other goodness-of-fit statistics, such as, the sum of squared errors (SSE), the R-square coefficient, and the root mean squared error (RMSE). For all considered combinations (s_i, s_e), surface fitting was computed on an underlying 65 x 65 grid, i.e., on a total of 4225 (σ_i, σ_e) pairs.

We observe that Table A.2 hints at the fact that $b_{s_i,s_e} = 1$ when $s_i = s_e$. One
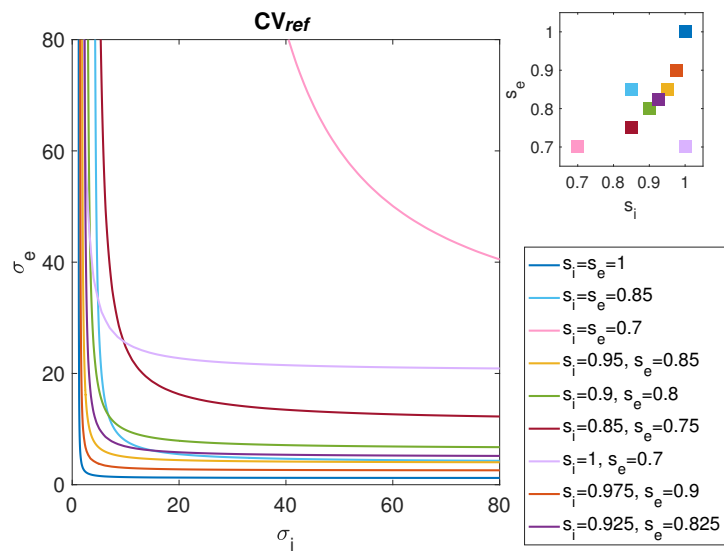
Figure 4: Differences in the location of the CV_{ref} isoline for various combinations of s_i and s_e. The colour-code of the main plot was also used to highlight the corresponding combinations of fractional parameters in (s_i, s_e) space in the top right of the figure (mirror combinations of off-diagonal (s_i, s_e) pairs and corresponding isolines not shown).

could in fact replace b with some constant $c^{s_i - s_e}$ without really affecting any of the fitting statistics except for the corresponding CI, which would in general become much larger due to the change in the order of magnitude of the considered constant.

In the spatially-homogeneous 1D case, $\sigma_e = \lambda \sigma_i$ for some $\lambda > 0$ always holds. Therefore, equation (11) can be rewritten as

$$
CV(\sigma_i, s_i, s_e) = a_{s_i, s_e} \left(\frac{\lambda^{s_e} \sigma_i^{s_i + s_e}}{b_{s_i, s_e} \sigma_i^{s_i} + \lambda^{s_e} \sigma_i^{s_e}} \right)^{\frac{1}{s_i + s_e}},
$$

which, under the assumption $s_e = s_i = s$ and by using that $b_s = 1$, reduces to

$$
CV(\sigma_i, s) = a_s \left(\frac{\lambda^s \sigma_i^{2s}}{(1 + \lambda^s)\sigma_i^s} \right)^{\frac{1}{2s}} = C_s \sqrt{\sigma_i},
$$

in perfect agreement with previously obtained results for the fractional Monodomain [1].

We remark that expression (11) is amenable to further generalisation in two- and three-dimensional domains.

3.3. Alternans dynamics and node formation

Having identified the same reference isoline for all considered combinations of fractional parameters, we are able to select suitable values of the conductivities in order to match the CV in all simulations. However, the following questions remain:

- Once CV has been matched, how do other experimentally relevant features of the travelling excitation wave, such as APD, vary as a function of different levels of non-locality in the fractional Bidomain?

- For a given combination of fractional parameters, are there qualitative and/or quantitative differences in the observed response to paced stimulation when σ_i and σ_e are varied along the same isoline?

- What is the effect (if any) of varying the domain size on the observed behaviour?

This section aims at answering the above questions and highlighting particular challenges that come into play when space-fractional non-locality is introduced in an already complex model formulation.

In order to address the above-mentioned questions, for each combination of s_i and s_e we identify a set of pairs (σ_i, σ_e) on the corresponding CV_{ref} isoline and run a different simulation for each of these parametric settings. All simulations consist in stimulating the cable via a dynamical protocol in which the pacing BCL is progressively reduced until $2 : 1$ response is observed (as described in detail in Section 2.5) and assessing spatio-temporal variations in APD, especially the insurgence of concordant or discordant alternans.

Figure 5 provides an example of the type of diagrams that were used to perform the analysis. In this particular simulation, the cable length is $L = 6$ cm, the fractional parameters are $s_i = s_e = 1$ (i.e., standard diffusion in both domains) and the conductivities are $\sigma_i = 3.25$ and $\sigma_e = 1.9$.

Figure 5 a) shows the mean APD along the cable for all beats of the dynamical protocol. The mean APD values for the n-th odd and n-th even beats are plotted in correspondence to the same abscissa, n, whose value has been omitted in these plots (as not truly informative). What has been indicated instead via the green horizontal axis is the value of the pacing cycle length (BCL) as it is reduced throughout the simulation and vertical lines denote the beat at which each reduction occurred. When vertical lines are close together, only a few beats were necessary to reach steady-state, while as pacing BCL was reduced and more complex dynamics emerged, the cable had to be paced for longer (i.e., for a larger number of consecutive beats) at the same BCL in order to reach stationarity. As one expects at low pacing frequency (i.e., at larger BCL), the average APD for odd and even beats is initially the same and slowly decreases as BCL is reduced. However, when pacing BCL is reduced below a certain "critical" value (here BCL $= 305$ ms), a marked difference (bifurcation) between odd and even beats emerges, likely indicating the insurgence of alternans (see below), and this difference is further increased with subsequent reductions of the BCL.

Figure 5 b) was built in a similar way in order to visualise variations in the maximum and minimum APD alternans (in absolute value) along the cable for all beats of the protocol. More specifically, absolute APD alternans for the n-th beat is here computed as the absolute difference between the n-th even and the n-th odd APD profiles in space. In the considered example, as we suspected when analysing Figure 5 a), alternans emerge at BCL $= 305$ ms and one can see that, while the maximum absolute alternans is large, the minimum is zero, thus indicating the presence of discordant alternans and of (at least) one node. The presence of concordant alternans could be similarly assessed but in that case, both minimum and maximum APD absolute alternans would be distinctively above zero (not shown).
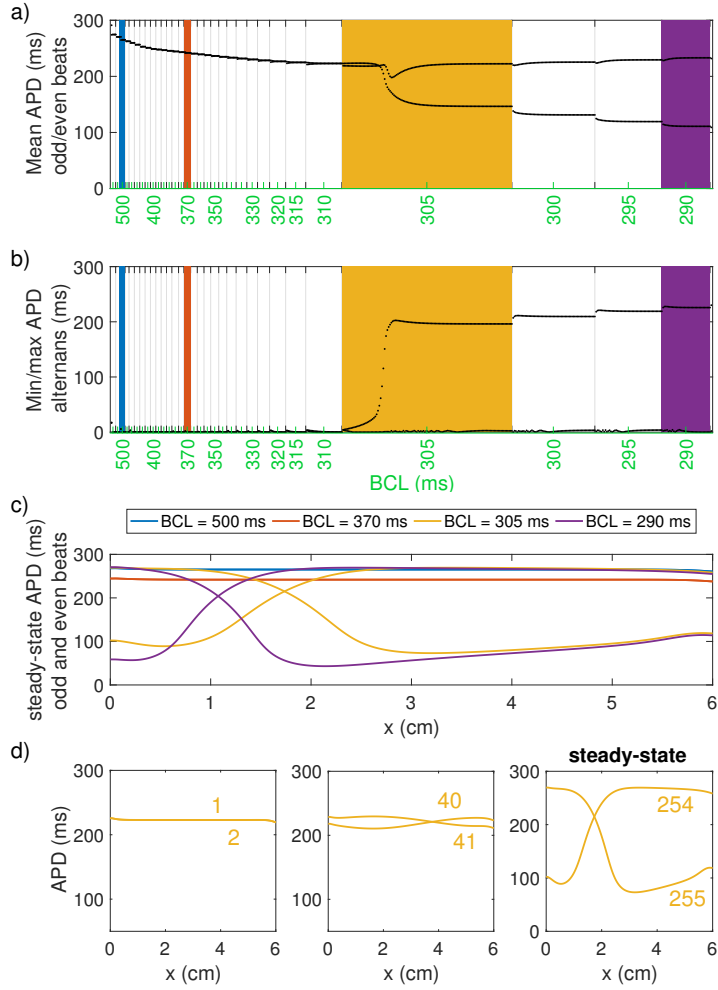
Figure 5: Dynamical restitution protocol for $s_i = s_e = 1$, $\sigma_i = 3.25$ and $\sigma_e = 1.9$, on a cable of length $L = 6$ cm. a) Mean APD along cable for all odd and even beats computed. b) Minimum and maximum APD alternans along cable for all beats. In both a) and b), vertical lines indicate change of pacing BCL (values reported in green). c) Steady-state APD of odd and even beats for four selected BCL, see highlighted regions of a) and b). d) Evolution of APD and insurgence of alternans at BCL = 305 ms (i.e., yellow region).

In order to confirm the qualitative behaviour expected after analysing Figures 5 a) and b), we could show on the same plot the steady-state APD along the considered cable at different pacing BCL. This is done in Figure 5 c) and the colour-code used to plot the stationary odd and even beats at each selected BCL is consistent with the colour used to highlight the portion of simulation results in a) and b) corresponding to the same BCL, namely, 500 ms (blue), 370 ms (orange), 305 ms (yellow), and 290 ms (purple). We can see that at larger BCL (500 and 370 ms) odd and even APD profiles are essentially indistinguishable but the mean APD corresponding to BCL = 370 ms is smaller than the one at 500 ms. For smaller values of BCL (305 and 290 ms) discordant alternans emerge, the maximum absolute amplitude of these alternans is larger at BCL = 290 ms, and the node moves closer to the pacing end of the cable as BCL is reduced.

Finally, to obtain further insight in the transition between absence and presence of alternans at the critical BCL (i.e, 305 ms), in Figure 5 d) we show three snapshots illustrating how the APD profiles change as the number of beats at the considered BCL increases (numbers reported in yellow indicate which particular APD profiles are shown in each plot).

Restitution surfaces for APD and local CV as a function of BCL and position along the cable could also be used to assess the complex spatio-temporal mechanisms underlying the formation of concordant and/or discordant alternans for different parameter combinations. A representative example is given in Figures A.9 and A.10 in the Appendix.

Due to the symmetric nature of the considered simplified problem, in all cases in which $s_i = s_e = s$, varying the conductivities along the reference isoline did not produce any qualitative nor quantitative change in the observed dynamics for that particular value of s.

However, this was no longer true when $s_i \neq s_e$, and even small deviations from the standard Bidomain case $s_i = s_e = 1$ (i.e., the introduction of mild levels of non-locality in both domains) exhibited interesting differences in the resulting dynamical response. An example of this is given in Figure 6, where three different combinations of σ_i, σ_e (labelled A, B, and C, respectively) are selected along the CV_{ref} isoline of the FBD with exponents $s_i = 0.975$ and $s_e = 0.9$. For each of these combinations the dynamical restitution protocol was applied on a cable of length $L = 9$ cm and the results are shown in three separate panels within the figure.

In each panel of Figure 6, we provide the evolution of mean APD of odd/even beats and minimum/maximum APD alternans throughout the performed simulation, as well as the steady-state APD profile in space for three selected BCL, corresponding to relevant changes in the observed dynamics for the example shown
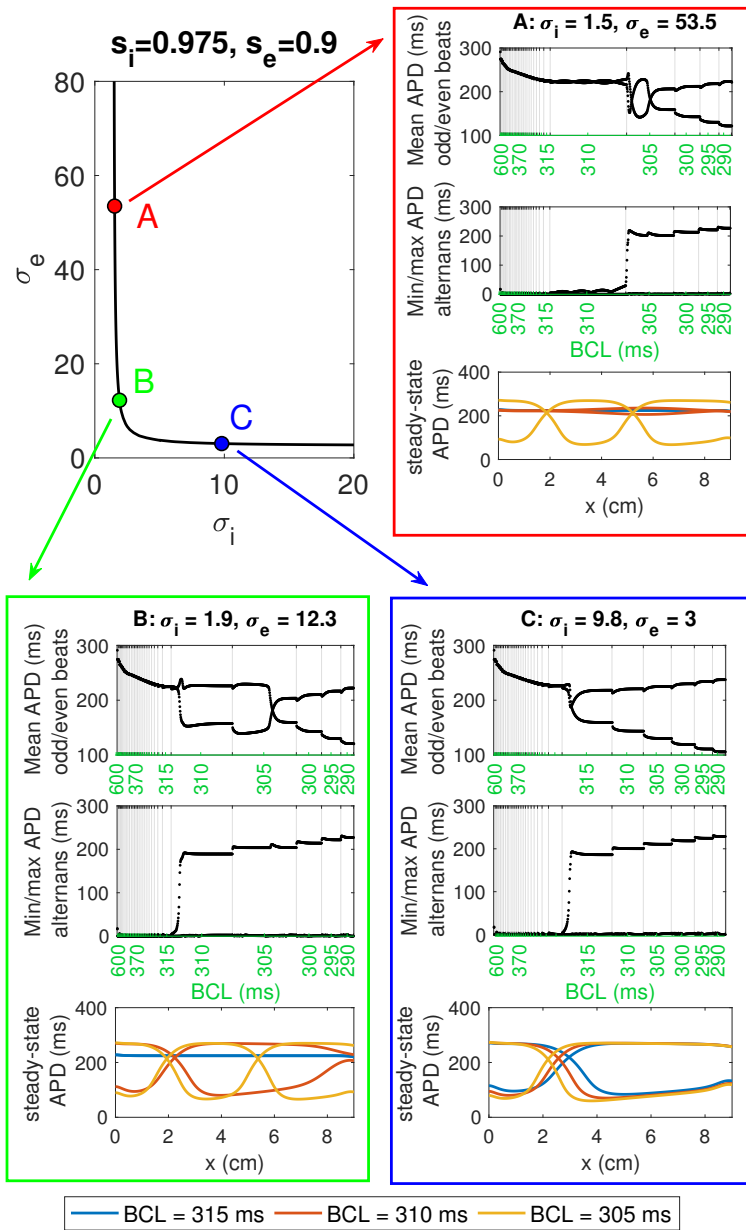
21

Figure 6: Dynamic behaviour and insurgence of alternans for three different combinations of (σ_i, σ_e) on the CV$_{\text{ref}}$ isoline of $s_i = 0.975, s_e = 0.9$.

here. In the red panel (point A: $\sigma_i = 1.5, \sigma_e = 53.5$), the mean APD starts exhibiting differences between odd and even beats at BCL = 310 ms, and these differences then become significantly larger at BCL = 305 ms. Similarly, small alternans appear at 310 ms while discordant alternans of much larger amplitude becomes visible at 305 ms. As shown by the steady-state profile, in this case there are two nodes forming along the cable (one around $x = 2$ cm and another one around $x = 5$ cm). In the green panel (point B: $\sigma_i = 1.9, \sigma_e = 12.3$), large discordant alternans emerge already at BCL = 310 ms, this time only with one node, and a second node forms when the BCL is further reduced to 305 ms. Finally, in the blue panel (point C: $\sigma_i = 9.8, \sigma_e = 3$), the onset of alternans is already at BCL = 315 ms, and while the alternans behaviour is discordant from then on, only one node forms and simply moves closer to the stimulated end of the cable as BCL is further reduced.

Overall we can already observe the following trends (which will be later confirmed with Figure 7): (i) onset of alternans happens at larger BCL when reducing the conductivity corresponding to the smaller fractional exponent, while (ii) the qualitative behaviour observed in the dynamic response becomes richer and more complex (i.e., two nodes instead of one in this case) as we move along the isoline in the opposite direction, that is, as the conductivity corresponding to the smaller fractional exponent increases. In order to better understand these trends, we performed a large number of simulations (on cables of two different lengths, namely $L = 9$ cm and $L = 6$ cm) and summarise the obtained results in Figure 7.

Figure 7 a) gives the BCL at which onset of alternans occurred for each combination of fractional parameters considered in this work, when varying both conductivities on the corresponding reference isoline. For completeness, in addition to the isolines corresponding to black and green points in Figure 1 b) (shown all together already in Figure 4) we also plot the isolines corresponding to mirror combinations of the fractional parameters (i.e., the red points in Figure 1 b)). Initially, 10 pairs of conductivities were selected per isoline but, in the cases $s_i \neq s_e$, additional intermediate points (up to 25 in total) were considered in order to obtain a refined picture of the dynamical variations observed, and linear interpolation was then used to smooth out colour variations along the entire curve. In both plots, we see that onset of alternas occurs at larger BCL when both conductivities are large and the isoline is thus further away from the axes. The critical BCL decreases when at least one of the conductivities can be reduced and for mixed combinations $s_i \neq s_e$ this occurs when decreasing the conductivity corresponding to the larger fractional exponent.

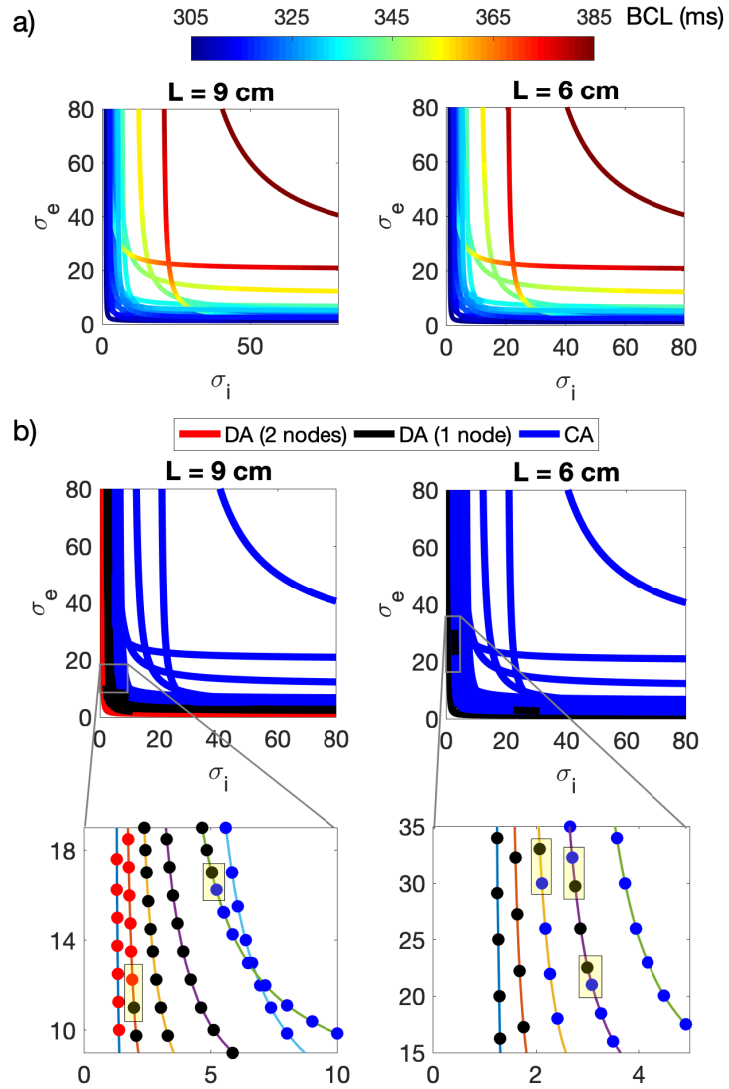Although very minor variations are present when comparing alternans onset

Figure 7: a) Pacing BCL at which alternans dynamics occurred when varying conductivities along the CV$_{\text{ref}}$ isoline for all considered combinations of s_i and s_e. b) Qualitative dynamic behaviour observed along the same isolines. Each considered (σ_i, σ_e) pair was classified according to the onset of concordant alternans (CA - blue) or discordant alternans (DA) exhibiting either one (black) or two (red) nodes. In both a) and b), results were obtained for a cable of length $L = 9$ cm (left) and $L = 6$ cm (right).

on the two cables (visible perhaps only in the transitions between green and yellow), the qualitative dynamical behaviour observed in the two cases is different, as shown in Figure 7 b). Here, for both cable lengths we use three different colours to identify the qualitative behaviour observed in the fast-pacing regime (i.e., short BCL) in correspondence of all selected nodes. Specifically, we distinguish between concordant alternans (blue) and discordant alternans with either one (black) or two (red) nodes. If during the dynamic protocol a transition between these states (e.g., discordant alternans with one and two nodes) was observed, only the final behaviour (i.e., discordant two nodes) was used in the classification of the considered node. As we can see, for both cable lengths the more complex dynamical behaviour occurs along the isolines that are closer to the axes. However, discordant alternans with two nodes only form on the $L = 9$ cm cable, indicating that richer dynamics typically occurs only when cable length is sufficiently large (a well-known fact for the standard diffusion case [55] and from experimental evidence [29, 6, 56, 57]). For both plots we "zoom in" into two regions of the parameter space exhibiting particularly interesting qualitative behaviour, that is, exhibiting transitions between alternans dynamics. In the bottom left plot, corresponding to the longer cable, for example, we highlight with a yellow rectangular selection the transition between discordant alternans with one and two nodes along the orange isoline ($s_i = 0.975, s_e = 0.9$) and the transition between concordant alternans and discordant alternans with one node on the green isoline ($s_i = 0.9, s_e = 0.8$). Similarly, in the bottom right plot corresponding to the $L = 6$ cm cable, we highlight the transition along the yellow isoline ($s_i = 0.95, s_e = 0.85$) and two transitions occurring on the purple isoline ($s_i = 0.925, s_e = 0.825$). Note that, in the "zoom in" plots only the isolines for green and black combinations of s_i and s_e of Figure 1 b) are plotted to facilitate visualisation, but all isolines were used to produce the full plots in the first two rows of the figure.

To complete this section we mention that we also investigated the role played by the particular choice of CV_{ref} on the above analysis on alternans dynamics and node formation. The selected value of $CV = 49.5$ cm s^{-1} corresponds in fact to fairly normal physiological conditions, while it is known that in pathological settings CV can be significantly reduced. The qualitative dynamic behaviour obtained on the isolines corresponding to a reduced reference CV, namely $CV_{ref} = 25$ cm s^{-1} are provided in Figure A.11. Once again we find that for $s_i \neq s_e$ the resulting dynamics depends on the particular selection of σ_i and σ_e along the reference isoline, whereas in the $s_i = s_e$ case no such differences are observed. However, as it is natural to expect, the slower starting CV allows a much richer dynamical behaviour on longer cables and the formation of alternans (in suitable

25

parametric settings) also on the shortest cable considered here (i.e., $L = 3$ cm). This feature is in line with recent spatio-temporal correlation analyses measuring and formulating the characteristic length of the action potential wave in the heart during regular pacing and alternans dynamics[11, 58].

4. Discussion

Even in healthy scenarios, cardiac tissue is a highly heterogeneous structure and discontinuities in electrical stimulus propagation arise on a variety of length scales. Intercellular electrical propagation, for example, is highly non-Ohmic due to the role played by gap junctions in the transmission of signal between connected myocytes, whereas the extracellular space is a complex mix of entities characterised by different conduction properties. Critical length-scales appear, in fact, as an emerging phenomenon of syncytium coordination. For example, the characteristic length of the tissue changes from around 40 cm during one-to-one responses down to about 3 cm at the transition from period-doubling bifurcation to fibrillation. Besides, spatio-temporal alternans regimes show consecutive oscillations of the normalised decay length which is critically linked to subcellular mechanisms regulating cell-cell communication. In such a scenario, the use of a model based on the homogenisation principle (i.e., based on the idea that there is a clear separation of scales between the level at which discontinuities arise and the level at which the transport phenomena is observed, thus implying that microscopic structure has negligible macroscopic effects) is questionable. This becomes even more important when analysing pathological scenarios typically associated with structural remodelling and significant enhancement of microscopic heterogeneity.

Fractional-order models have successfully been used to reproduce macroscopic effects accounting for microscopic heterogeneities, without the need to resolve complex spatial structures down to the microscopic level. As the use of space-fractional operators in the context of cardiac modelling is a relatively recent approach (which presents its own mathematical challenges), several aspects have yet to be clarified, especially in relation to the formulation of physically meaningful models for a robust and reasonable comparison with experimental data.

So far, the space-fractional approach has been used only to generalise the classical Monodomain model. In this work, we propose a space-fractional Bidomain formulation based on a spectral representation of the diffusion operators for electrical propagation of stimuli through the intra- and extra-cellular domains, and we perform a simulation study in order to investigate fundamental properties of

the derived model. In order to understand the interplay between model parameters and relevant quantities of interest, we consider the newly formulated FBD in simplified computational settings (i.e., 1D with spatially constant conductivities) and leave the analysis of more complex geometries with possibly anisotropic characteristics for future investigation.

The presented work highlights the symmetric role of fractional exponents and conductivity parameters of the FBD in the considered simplified settings, it generalises previously established results obtained by the authors on the dependency of the CV at low pacing frequency for the fractional Monodomain, and highlights critical differences in APD behaviour following dynamical pacing observed for different parametric combinations with initially matched CV. While the particular choice of conductivities along a selected isoline does not affect APD dynamics for the classical Bidomain formulation (as for all other choices of equal fractional exponents characterising the two domains), this is no longer true when $s_i \neq s_e$. In these settings, in fact, we observed that the asymmetry of the reference CV isoline in parametric space translates into different dynamical scenarios depending on the particular choice of the (σ_i, σ_e) pair, with larger values of the conductivity parameter corresponding to the highest fractional exponent typically giving richer dynamics in terms of alternans and node formation. This adds to the challenges already existing for the classical Bidomain formulation in the proper estimation of suitable conductivities [59] and undoubtedly requires further investigation in higher spatial dimensions to better elucidate the effects of non-locality in either (or both) spatial domains. Finally, in line with well-established results for the standard case, for any particular parameter combination of the FBD we observe richer dynamical responses (allowing the formation of discordant alternans - if previously absent - and potentially increasing the number of nodes formed at a given BCL) when increasing the cable length or reducing the reference CV.

Besides the simplified settings and low dimensionality of the considered problem, one important limitation of the present work is the particular selection of the Beeler-Reuter model for the description of the underlying cellular mechanisms at the single-cell level. The alternans dynamics observed in this work is essentially related to the APD restitution properties and to the changes observed in APD restitution as a function of the fractional parameters in the FBD. However, intracellular calcium handling is known to be another important factor of alternans dynamics, independent from APD restitution [3, 60]. The Beeler-Reuter cellular description explicitly models intra-cellular calcium, but its dynamics is in essence zero-dimensional. Therefore, when we analysed calcium variations in tissue (results not shown), we observed alternans that are intrinsically voltage-driven and very

much exhibit the same qualitative features observed here for the APD. Working with a model allowing for both voltage- and calcium-driven alternans is important and will surely be considered by us for future investigation in this direction.

From a multi-scale modeling perspective, the present contribution drives attention to complex emergent dynamics due to intra- and inter-cellular couplings in excitable systems. Specifically, non-local connectivity is known to distinguish cellular syncytia due to gap junction and functional networks behavior [61, 62, 63, 64, 65]. We aim, therefore, to further stimulate the community in investigating complex emerging phenomena in cardiac electrophysiology in view of a more effective translation of a scientific rationale into the clinical practice.

Acknowledgements

Data availability statement

The data that support the findings of this study are available from the corresponding author upon reasonable request.

[1] N. Cusimano, A. Gizzi, F. H. Fenton, S. Filippi, L. Gerardo-Giorda, Key aspects for effective mathematical modelling of fractional-diffusion in cardiac electrophysiology: A quantitative study, Communications in Nonlinear Science and Numerical Simulation 84 (2020) 105152.

[2] N. A. Trayanova, A. N. Doshi, A. Prakosa, How personalized heart modeling can help treatment of lethal arrhythmias: A focus on ventricular tachycardia ablation strategies in post-infarction patients, Wiley Interdisciplinary Reviews: Systems Biology and Medicine (2020) e1477.

[3] T. You, C. Luo, K. Zhang, H. Zhang, Electrophysiological mechanisms underlying t-wave alternans and their role in arrhythmogenesis, Frontiers in Physiology 12 (2021) 235.

[4] S. A. Niederer, N. A. T. J. Lumens, Computational models in cardiology, Nat. Rev. Cardiol. 16 (2019) 100–111.

[5] V. Biasci, L. Sacconi, E. N. Cytrynbaum, D. A. Pijnappels, T. D. Coster, A. Shrier, L. Glass, G. Bub, Universal mechanisms for self-termination of rapid cardiac rhythm, Chaos 30 (2020) 121107.

[6] A. Gizzi, E. Cherry, R. F. G. Jr., S. Luther, S. Filippi, F. H. Fenton, Effects of pacing site and stimulation history on alternans dynamics and the development of complex spatiotemporal patterns in cardiac tissue, Front. Physiol 71 (2013) 4.

[7] Z. Qu, G. Hu, A. Garfinkel, J. N.Weiss, Nonlinear and stochastic dynamics in the heart, Phys. Rep. 543 (2014) 61–162.

[8] G. Hu, Z. Song, J. Landaw, Z. Qu, Spatially discordant repolarization alternans in the absence of conduction velocity restitution, Biophys. J. 118 (2020) 2574–2587.

[9] W. A. Ramirez, A. Gizzi, K. L. Sack, J. M. Guccione, D. E. Hurtado, In-silico study of the cardiac arrhythmogenic potential of biomaterial injection therapy, Sci. Rep. 10 (2020) 1–14.

[10] S. Pezzuto, A. Gharaviri, U. Schotten, M. Potse, G. Conte, M. L. Caputo, F. Regoli, R. Krause, A. Auricchio, Beat-to-beat p-wave morphological variability in patients with paroxysmal atrial fibrillation: an in silico study, EP Europace 20 (3) (2018) iii26–iii35.

[11] A. Loppini, A. Gizzi, C. Cherubini, E. M. Cherry, F. H. Fenton, S. Filippi, Spatiotemporal correlation uncovers fractional scaling in cardiac tissue, Physical Review E 103 (2019) 020201.

[12] D. Bini, C. Cherubini, S. Filippi, A. Gizzi, P. E. Ricci, On spiral waves arising in natural systems, Comm. Comput. Phys. 8 (2010) 610.

[13] C. Huang, Z. Song, Z. Di, Z. Qu, Stability of spatially discordant repolarization alternans in cardiac tissue, Chaos: An Interdisciplinary Journal of Nonlinear Science 30 (12) (2020) 123141.

[14] M. A. Colman, The multiple mechanisms of spatially discordant alternans in the heart, Biophysical Journal 118 (10) (2020) 2336–2338.

[15] L. M. Munoz, A. R. M. Gelzer, F. H. Fenton, W. Qian, W. Lin, R. F. G. Jr, N. F. Otani, Discordant alternans as a mechanism for initiation of ventricular fibrillation in vitro, J Am Heart Assoc. 7 (2018) e007898.

[16] H. V. Perez, F. H. Fenton, Low dimensional structures in cardiac alternans, Bulletin of the American Physical Society 65.

[17] A. Barone, F. H. Fenton, A. Veneziani, Numerical sensitivity analysis of a variational data assimilation procedure for cardiac conductivities, Chaos: An Interdisciplinary Journal of Nonlinear Science 27 (9) (2017) 093930.

[18] A. Quaglino, S. Pezzuto, P. S. Koutsourelakis, A. Auricchio, R. Krause, Fast uncertainty quantification of activation sequences in patient-specific cardiac electrophysiology meeting clinical time constraints, Int J Numer Method Biomed Eng 34 (7) (2018) e2985.

[19] A. Barone, A. Gizzi, F. H. Fenton, S. Filippi, A. Veneziani, Experimental validation of a variational data assimilation procedure for estimating space-dependent cardiac conductivities, Comput. Method Appl. Mech. Eng. 358 (2020) 112615.

[20] P. Pathmanathan, S. Galappaththige, J. Cordeiro, A. Kaboudian, F. Fenton, R. Gray, Data-driven uncertainty quantification for cardiac electrophysiological models: Impact of physiological variability on action potential and spiral wave dynamics, Frontiers in Physiology 11 (2020) 585400.

[21] A. Barone, M. G. Carlino, A. Gizzi, S. Perotto, A. Veneziani, Efficient estimation of cardiac conductivities: A proper generalized decomposition approach, J. Comput. Phys. 423 (2020) 109810.

[22] C. D. Marcotte, F. H. Fenton, M. J. Hoffman, E. M. Cherry, Robust data assimilation with noise: Applications to cardiac dynamics, Chaos: An Interdisciplinary Journal of Nonlinear Science 31 (2021) 013118.

[23] C. S. Henriquez, Simulating the electrical behavior of cardiac tissue using the bidomain model, Crit Rev Biomed Eng 21 (1993) 1–77.

[24] R. H. Clayton, O. Bernus, E. M. Cherry, H. Dierckx, F. H. Fenton, L. Mirabella, A. V. Panfilov, F. B. Sachse, G. Seeman, H. Zhang, Models of cardiac tissue electrophysiology: Progress challenges and open questions, Prog. Biophys. Mol. Biol. 104 (2011) 22–48.

[25] M. Potse, B. Dubé, J. Richer, A. Vinet, A comparison of monodomain and bidomain reaction-diffusion models for action potential propagation in the human heart, IEEE Transactions on Biomedical Engineering 53 (2006) 2425–2435.

[26] J. P. W. Jr., S.-F. Lin, R. A. Abbas, Virtual electrodes in cardiac tissue: a common mechanism for anodal and cathodal stimulation, Biophysical Journal 69 (1995) 2195–2210.

[27] I. R. Efimov, R. A. Gray, B. J. Roth, Virtual electrodes and deexcitation: new insights into fibrillation induction and defibrillation, Journal of Cardiovascular Electrophysiology 11 (2000) 339–353.

[28] S. Luther, F. H. Fenton, B. G. Kornreich, A. Squires, P. Brittihn, D. Hornung, M. Zabel, J. Flanders, A. Glanduli, L. Campoy, E. M. Cherry, G. Luther, G. Hasenfuss, V. I. Krinsky, A. Pumir, R. F. Gilmour Jr, E. Bodenschatz, Low-energy control of electrical turbulence in the heart, Nature 475 (2011) 235–239.

[29] A. Loppini, A. Gizzi, R. R. Baier, C. Cherubini, F. H. Fenton, S. Filippi, Competing mechanisms of stress-assisted diffusivity and stretch-activated currents in cardiac electromechanics, Front. Physiol. 9 (2018) 1714.

[30] D. J. Christini, M. L. Riccio, C. A. Culianu, J. J. Fox, A. Karma, R. F. Gilmour, Control of electrical alternans in canine cardiac purkinje fibers, Phys. Rev. Lett. 96 (2006) 104101.

[31] T. Krogh-Madsen, A. Karma, M. L. Riccio, P. N. Jordan, D. J. Christini, J. R. F. Gilmour, Off-site control of repolarization alternans in cardiac fibers, Phys. Rev. E 81 (2010) 011915.

[32] N. Wei, Y. Mori, E. G. Tolkacheva, The dual effect of ephaptic coupling on cardiac conduction with heterogeneous expression of connexin 43, J. Theor. Biol. 397 (2016) 103–114.

[33] S. H. Weinberg, Ephaptic coupling rescues conduction failure in weakly coupled cardiac tissue with voltage-gated gap junctions, Chaos 27 (2017) 093908.

[34] D. E. Hurtado, S. Castro, A. Gizzi, Computational modeling of non-linear diffusion in cardiac electrophysiology: A novel porous-medium approach,

Computer Methods in Applied Mechanics and Engineering 300 (2016) 70–83.

[35] C. Cherubini, S. Filippi, A. Gizzi, R. Ruiz-Baier, A note on stress-driven anisotropic diffusion and its role in active deformable media, J. Theor. Biol. 430 (2017) 221–228.

[36] A. Gizzi, et. al., Nonlinear diffusion and thermo-electric coupling in a two-variable model of cardiac action potential, Chaos: An Interdisciplinary Journal of Nonlinear Science 27 (2017) 093919.

[37] D. E. Hurtado, J. Jiliberto, G. Panasenko, Non-ohmic tissue conduction in cardiac electrophysiology: upscaling the non-linear voltage-dependent conductance gap junctions, PLoS Computational Biology 16 (2020) e1007232.

[38] A. Bueno-Orovio, D. Kay, V. Grau, B. Rodriguez, K. Burrage, Fractional diffusion models of cardiac electrical propagation: role of structural heterogeneity in dispersion of repolarization, J. R. Soc. Interface 11 (2014) 20140352.

[39] N. Cusimano, A. Bueno-Orovio, I. Turner, K. Burrage, On the order of the fractional laplacian in determining the spatio-temporal evolution of a space-fractional model of cardiac electrophysiology, PLoS ONE 10 (2015) e0143938.

[40] N. Cusimano, L. Gerardo-Giorda, A space-fractional Monodomain model for cardiac electrophysiology combining anisotropy and heterogeneity on realistic geometries, J. Comp. Phys. 362 (2018) 409–424.

[41] Y. Wang, L. Cai, X. Feng, X. Luo, H. Gao, A ghost structure finite difference method for a fractional fitzhugh-nagumo monodomain model on moving irregular domain, Journal of Computational Physics 428 (2021) 110081.

[42] T. Comlekoglu, S. H. Weinberg, Memory in a fractional-order cardiomyocyte model alters properties of alternans and spontaneous activity, Chaos 27 (2017) 093904.

[43] T. Comlekoglu, S. H. Weinberg, Memory in a fractional-order cardiomyocyte model alters voltage- and calcium-mediated instabilities, Communications in Nonlinear Science and Numerical Simulations 89 (2020) 105340.

[44] J. P. Ugarte, C. Tobón, A. M. Lopes, J. A. T. Machado, Atrial rotor dynamics under complex fractional order diffusion, Frontiers in Physiology 9 (2018) 975.

[45] J. P. Ugarte, C. Tobón, A. M. Lopes, J. A. T. Machado, A complex order model of atrial electrical propagation from fractal porous cell membrane, Fractals 28 (2020) 2050106–1678.

[46] P. Lenarda, A. Gizzi, M. Paggi, A modeling framework for electro-mechanical interaction between excitable deformable cells, European Journal of Mechanics-A/Solids 72 (2018) 374–392.

[47] L. M. Treml, E. Bartocci, A. Gizzi, Modeling and analysis of cardiac hybrid cellular automata via GPU-accelerated Monte Carlo simulation, Mathematics 9 (2021) 164.

[48] Y. Shiferaw, M. A. Watanabe, A. Garfinkel, J. N. Weiss, A. Karma, Model of intracellular calcium cycling in ventricular myocytes, Biophys. J. 85 (2003) 3666–3686.

[49] L. Romero, E. Alvarez-Lacalle, Y. Shiferaw, Stochastic coupled map model of subcellular calcium cycling in cardiac cells, Chaos: An Interdisciplinary Journal of Nonlinear Science 29 (2019) 023125.

[50] P. Pathmanathan, M. O. Bernabeu, R. Bordas, J. Cooper, A. Garny, J. M. Pitt-Francis, J. P. Whiteley, D. J. Gavaghan, A numerical guide to the solution of the bidomain equations of cardiac electrophysiology, Progress in Biophysics and Molecular Biology 102 (2010) 136–155.

[51] N. Cusimano, F. del Teso, L. Gerardo-Giorda, Numerical approximations for fractional elliptic equations via the method of semigroups, EASIM: M2AN 54 (2020) 751–774.

[52] G. W. Beeler, H. Reuter, Reconstruction of the action potential of ventricular myocardial fibres, J. Physiol. 268 (1977) 177–210.

[53] A. Bueno-Orovio, D. Kay, K. Burrage, Fourier spectral methods for fractional-in-space reaction-diffusion equations, BIT Num. Math. 54 (2014) 937–954.

[54] K. N. Aronis, R. L. Ali, A. Prakosa, H. Ashikaga, R. D. Berger, J. B. Hakim, J. Liang, H. Tandri, F. Teng, J. Chrispin, N. A. Trayanova, Accurate conduction velocity maps and their association with scar distribution on magnetic resonance imaging in patients with postinfarction ventricular tachycardias, Circulation: Arrhythmia and Electrophysiology 13 (2020) e007792.

[55] M. A. Watanabe, F. H. Fenton, S. J. Evans, H. M. Hastings, A. Karma, Mechanisms for discordant alternans, J. Cardiovasc. Electrophysiol. 12 (2002) 196–206.

[56] A. Gizzi, A. Loppini, E. Cherry, C. Cherubini, F. H. Fenton, S. Filippi, Multi-band decomposition analysis: application to cardiac alternans as a function of temperature, Physiol. Measurement 38 (2017) 833.

[57] I. Uzelac, Y. Ji, D. Hornung, J. Schröder-Scheteling, S. Luther, R. Gray, E. Cherry, F. Fenton, Simultaneous quantification of spatially discordant alternans in voltage and intracellular calcium in langendorff-perfused rabbit hearts and inconsistencies with models of cardiac action potentials and ca transients, Frontiers in Physiology 8 (2017) 819.

[58] A. Loppini, A. Barone, A. Gizzi, C. Cherubini, F. H. Fenton, S. Filippi, Thermal effects on cardiac alternans onset and development: A spatiotemporal correlation analysis, Physical Review E 103 (2021) L040201.

[59] B. Johnston, P. Johnston, Approaches for determining cardiac bidomain conductivity values: progress and challenges, Medical & Biological Engineering & Computing 58 (2020) 2919—2935.

[60] A. Garfinkel, Eight (or more) kinds of alternans, J. Electrocardiol. 40 (2007) S70–S74.

[61] M. Bertolaso, A. Capolupo, C. Cherubini, S. Filippi, A. Gizzi, A. Loppini, G. Vitiello, The role of coherence in emergent behavior of biological systems, Electromagnetic Biology and Medicine 34 (2015) 138–140.

[62] A. Loppini, S. Filippi, H. E. Stanley, Critical transitions in heterogeneous networks: Loss of low-degree nodes as an early warning signal, Phys Rev E 99 (2019) 040301.

[63] H. Ashikaga, R. G. James, Inter-scale information flow as a surrogate for downward causation that maintains spiral waves, Chaos 28 (2018) 075306.

[64] A. Loppini, M. G. Pedersen, Gap-junction coupling can prolong beta-cell burst period by an order of magnitude via phantom bursting, Chaos: An Interdisciplinary Journal of Nonlinear Science 28 (2018) 063111.

[65] A. Loppini, C. Cherubini, M. Bertolaso, S. Filippi, Breaking down calcium timing in heterogenous cells populations, Biosystems 191 (2018) 104117.

Appendix A. Additional tables and figures

Table A.1: Rough number of simulations (i.e., different parametric combinations) considered for the results presented in this work and corresponding estimate of the computation time required for each of these simulations.

Objective	CV_{ref}	# Simulations	Time per simulation
CV surface analysis and iso-lines identification	45.9	34500	1 to 2 minutes
	other	42250	3 to 5 minutes
Dynamic protocol response and alternans analysis	49.5	300	1 to 4 hours
	25	150	2.5 to 15 hours

Table A.2: Fitting constants for equation (11) and corresponding goodness-of-fit statistics.

s_i	s_e	a_{s_i,s_e}	CI	b_{s_i,s_e}	CI	SSE	R-squared	RMSE
1	1	46.75	[46.74,46.76]	1	[0.999,1.001]	165.4	1	0.1979
1	0.85	46.18	[46.08,46.29]	2.609	[2.594,2.624]	3582	0.9981	0.921
0.975	0.9	42.33	[42.29,42.36]	1.602	[1.599,1.606]	922.4	0.9996	0.4674
0.95	0.85	38.59	[38.54,38.64]	1.934	[1.927,1.940]	1383	0.9992	0.5723
0.925	0.825	35.04	[34.99,35.10]	1.975	[1.967,1.982]	1279	0.999	0.5503
0.85	0.85	25.67	[25.65,25.69]	1	[0.998,1.002]	367.3	0.9997	0.2949

Table A.3: Combinations of parameters used to produce the solution profiles of Figure A.8

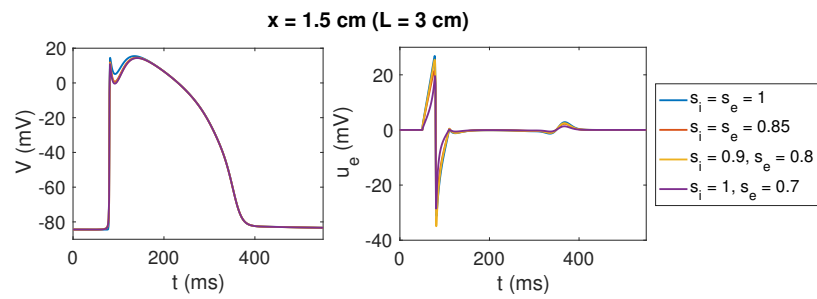| s_i	s_e	σ_i	σ_e
1	1	3.25	1.9
0.85	0.85	10.5	7.61
0.9	0.8	11.5	9.28
1	0.7	4.03	37

Figure A.8: Action potential (left) and extra-cellular potential profile (right) at the mid-point of a 3 cm long cable for four different parametric combinations. Conductivities have been tuned to produce the same CV in all cases.
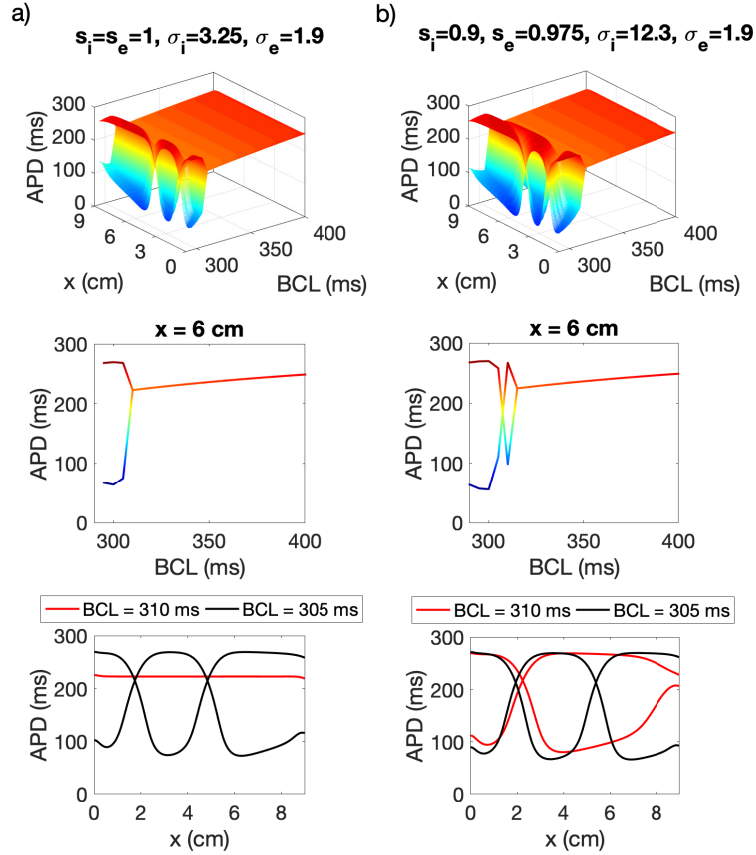
Figure A.9: APD restitution surfaces (top row) and 2D cross-sectional visualisations along different vertical planes (second row: $x = 6$ cm, third row red: BCL = 310 ms, third row black: BCL = 305 ms) for two different parameter combinations, namely, column a) $s_i = s_e = 1, \sigma_i = 3.25, \sigma_e = 1.9$ and column b) $s_i = 0.9, s_e = 0.975, \sigma_i = 12.3, \sigma_e = 1.9$.

Figure A.10: CV restitution surfaces (top row) and 2D cross-sectional visualisations along different vertical planes (second row: $x = 6$ cm, third row red: BCL $= 310$ ms, third row black: BCL $= 305$ ms) for two different parameter combinations, namely, column a) $s_i = s_e = 1, \sigma_i = 3.25, \sigma_e = 1.9$ and column b) $s_i = 0.9, s_e = 0.975, \sigma_i = 12.3, \sigma_e = 1.9$.
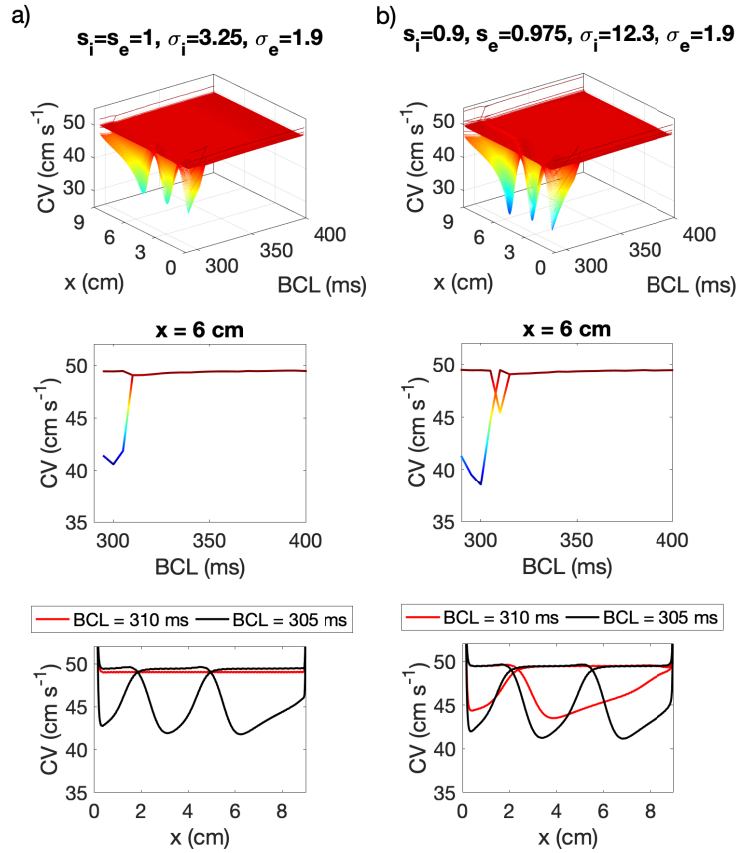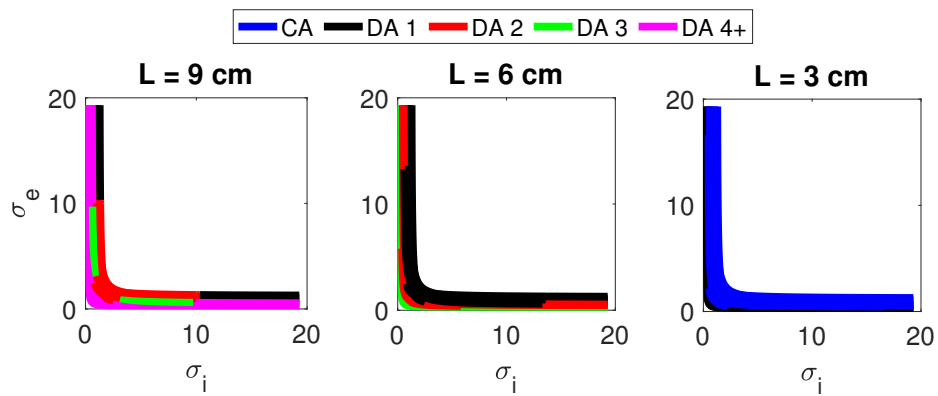
Figure A.11: Qualitative dynamic behaviour observed along the isoline $CV = 25$ cm s^{-1}. Each considered (σ_i, σ_e) pair was classified according to the onset of concordant alternans (CA - blue) or discordant alternans (DA) exhibiting either one (black), two (red), three (green) or more (magenta) nodes. Three cable lenghts ($L = 3, 6, 9$ cm) and five different (s_i, s_e) pairs were considered to generate these plots.